Magmatic and tectonic extension at the Chile Ridge: Evidence for mantle controls on ridge segmentation

Samuel M. Howell[1], Garrett Ito[1], Mark D. Behn[2], Fernando Martinez[3], Jean-Arthur Olive[4], and Javier Escartín[5]

[1]Department of Geology and Geophysics, University of Hawaii at Manoa, Honolulu, Hawaii, USA, [2]Department of Geology and Geophysics, Woods Hole Oceanographic Institution, Woods Hole, Massachusetts, USA, [3]Hawaii Institute of Geophysics and Planetology, University of Hawaii at Manoa, Honolulu, Hawaii, USA, [4]Marine Geology and Geophysics, Lamont-Doherty Earth Observatory, Palisades, New York, USA, [5]Marine Geosciences, CNRS/Institut de Physique du Globe de Paris, Paris, France

Abstract We use data from an extensive multibeam bathymetry survey of the Chile Ridge to study tecto-nomagmatic processes at the ridge axis. Specifically, we investigate how abyssal hills evolve from axial faults, how variations in magmatic extension influence morphology and faulting along the spreading axis, and how these variations correlate with ridge segmentation. The bathymetry data are used to estimate the fraction of plate separation accommodated by normal faulting, and the remaining fraction of extension, M, is attributed primarily to magmatic accretion. Results show that M ranges from 0.85 to 0.96, systematically increasing from first-order and second-order ridge segment offsets toward segment centers as the depth of ridge axis shoals relative to the flanking highs of the axial valley. Fault spacing, however, does not correlate with ridge geometry, morphology, or M along the Chile Ridge, which suggests the observed increase in tectonic strain toward segment ends is achieved through increased slip on approximately equally spaced faults. Variations in M along the segments follow variations in petrologic indicators of mantle melt fraction, both showing a preferred length scale of 50 ± 20 km that persists even along much longer ridge segments. In comparison, mean M and axial relief fail to show significant correlations with distance offsetting the segments. These two findings suggest a form of magmatic segmentation that is partially decoupled from the geometry of the plate boundary. We hypothesize this magmatic segmentation arises from cells of buoyantly upwelling mantle that influence tectonic segmentation from the mantle, up.

1. Introduction

The origin of abyssal hills and the morphology of mid-ocean ridges has long been a subject of interest [e.g., *Macdonald*, 1982, 1986], and many workers have contributed to an evolving understanding of the critical underlying processes. The earliest, first-order observation was that fault-generated abyssal hills and ridge morphology differ drastically with spreading rate. Slow spreading ridges are characterized by kilometers-wide axial valleys flanked by shallow topography, and $\sim 10^3$ m tall abyssal hills comprised of one or more normal faults, whereas fast spreading ridges exhibit relatively smooth, topographically high axial ridges, and $\sim 10^2$ m tall fault topography [e.g., *Goff et al.*, 1997; *Macdonald*, 1982; *Searle and Laughton*, 1981; *Small*, 1998].

To understand these differences, many studies have investigated the role of dynamic lithospheric stresses [e.g., *Chen and Morgan*, 1990a, 1990b; *Lin and Parmentier*, 1989; *Tapponnier and Francheteau*, 1978]. Early modeling efforts by *Chen and Morgan* [1990a] showed that axial valleys are supported by dynamic stresses, and the magnitude of axial valley relief that the stresses can support increases with axial lithospheric thickness. Their models predicted slow spreading ridges to have thick lithosphere, and thus deep axial valleys, and fast spreading ridges to have thin lithosphere and minimal dynamic stresses that yield a nearly isostatically supported axial topographic high. Closely following this work, *Chen and Morgan* [1990b] and *Phipps Morgan and Chen* [1993a, 1993b] were seminal in quantifying the links between lithosphere thickness and magmatism. These studies showed that the low magma flux at slow spreading ridges delivers a reduced heat flux to the ridge axis, which—combined with efficient hydrothermal cooling—leads to a thicker axial lithosphere. Conversely, the relatively high magma heat flux delivered to fast spreading ridges was

predicted to lead to thin lithosphere. These heat balance arguments further reinforced the concept that lithospheric thickness and stresses control the differing styles of faulting and axial morphology.

Within this context, numerous studies have investigated the sources of variations in faulting and morphology along mid-ocean ridge spreading segments. One motivating observation at some slow and intermediate spreading ridges is that near segment ends, axial valleys tend to be deeper and flanked by larger and more widely spaced faults than near segment centers [*Chen and Morgan*, 1990b; *Shaw*, 1992; *Shaw and Lin*, 1993]. Additionally, workers discovered geophysical evidence for thinner crust, and hence lower magma supply, near segment ends compared to segment centers [*Forsyth*, 1992; *Kuo and Forsyth*, 1988; *Lin and Phipps Morgan*, 1992; *Lin et al.*, 1990], as later shown seismically at the Mid-Atlantic Ridge [*Dunn et al.*, 2005; *Hooft et al.*, 2000; *Tolstoy et al.*, 1993]. To better understand these observations, *Shaw and Lin* [1996] included the effect of along-axis variations in melt supply and mantle flow in three-dimensional thermal models of segmented ridges. At slow spreading rates, their thermal models predicted that segment ends are characterized by thicker axial lithosphere than segment centers, and their cyclic models of faulting showed a corresponding increase in fault slip and axial valley depth toward segment ends.

An important shift in our understanding of the linkage between magma flux, faulting, and axial morphology began with early concepts of *Shaw and Lin* [1993], who suggested that the ratio of magmatic to amagmatic spreading is an important control on faulting. The kinematic arguments and fully dynamic models of *Buck et al.* [2005] demonstrated that the most direct control on the size and spacing of faults is the fraction of extension accommodated by magmatic emplacement, M, and not the influence of magmatism on axial thermal structure. Subsequent studies confirmed the direct response of faulting to M [e.g., *Behn and Ito*, 2008; *Ito and Behn*, 2008; *Tucholke et al.*, 2008], and *Ito and Behn* [2008] further demonstrated that M directly influences axial topography because, in a time-averaged sense, M controls the magnitude of the dynamic lithospheric stresses identified by *Chen and Morgan* [1990a, 1990b] (tensile stress is relieved during periods of magmatic extension and enhanced during periods of tectonic extension). Changes in M from relatively low to high values lead to a transition from deep axial valleys to shallow axial topographic highs, with intermediate values producing transitional axial topography similar to that observed at intermediate spreading ridges. Whereas M is becoming recognized as the most direct control on fault characteristics and ridge morphology, relatively few studies have quantified this fraction at mid-ocean ridges and explored how variations in M between and within segments correlate with variations in ridge characteristics [*Escartín et al.*, 1999; *Ito and Behn*, 2008; *Paulatto et al.*, 2015; *Schouten et al.*, 2010].

This study aims to quantify variations in faulting, axial valley relief, and ridge geometry to understand the relationships among M, fault characteristics and evolution, plate boundary geometry, and axial morphology at the intermediate spreading Chile Ridge (Figure 1). The Chile Ridge strikes northwest from the southern coast of Chile, and has spread relatively uniformly (31 km/Myr half spreading rate) since at least 5.9 Ma [*Tebbens et al.*, 1997]. All spreading segments are orthogonal to the spreading direction, facilitating their identification. Additionally, the wide range of segment lengths and offset distances in this ridge section make it well suited to study the effects of segmentation geometry. To address these issues, we first measure ridge segment length, segment offset distance, axial relief, and individual fault throws and dips at five first-order (bounded by transform faults) and four second-order (bounded by oblique shear zones and axial valley jogs [*Macdonald et al.*, 1991a]) ridge segments. We then estimate the fraction of plate separation taken up by prominent, lithosphere-scale normal faults (Figure 2), and consider the remaining, unaccounted fraction of extension, M, to be a proxy for magmatic accretion. Finally, we compare segment-scale variations in M with variations in seafloor chemistry. Our results provide evidence for the mechanisms by which small axial faults evolve into abyssal hills, elucidate how variations in magmatic extension influence fault characteristics and ridge morphology, and relate magmatic and tectonic segmentation to the style of mantle upwelling beneath this intermediate spreading ridge.

2. Tectonic Setting

The Chile Ridge extends southeast from the junction of the Pacific, Antarctic, and Nazca plates at the Juan Fernandez microplate to the triple junction of the Antarctic, Nazca, and South American plates (Figure 1) [*Tebbens et al.*, 1997, and references therein]. The proximity of the Chile Ridge to the equator of its Euler pole yields a relatively uniform half-spreading rate of ∼31 km/Myr along its length since 5.9 Ma [*Tebbens*
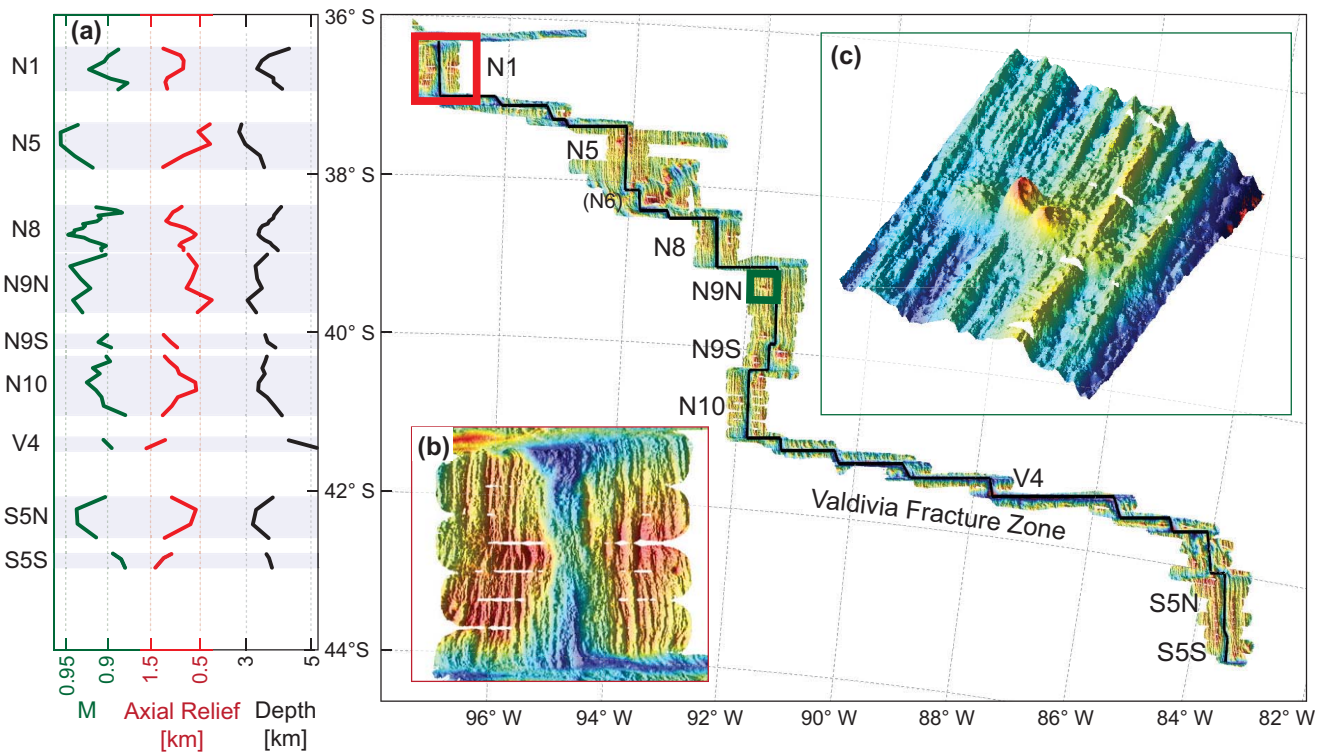
Figure 1. Multibeam bathymetry and along-axis variability of the Chile Ridge. (a) Along-axis variations in the ratio of the fraction of total extension accommodated magmatically, M (green), axial valley relief, the depth of the axial valley floor below the flanking topographic highs after removing the short-wavelength topography due to faulting (red), and axial valley floor depth (black). First-order spreading segments are labeled and highlighted with grey boxes. The red square around segment N1 marks the area showing (b) an example of a classic hourglass morphology, characterized by depth contours (e.g., the light blue color) that are far apart near the deep segment ends and become closer together near the shallow segment center. The green square around the northwest quadrant of segment N9N marks (c) the area of a short volcano chain interrupting the continuity of axis-parallel faults.

et al., 1997]. The spreading segments range in length from <20 to >200 km, and are offset from each other by distances of ~10 to >1100 km.

The Chile Ridge is separated into northern and southern sections by the transform-dominated Valdivia Fracture Zone, which offsets the two sections of the ridge by more than 600 km east-to-west. The northern section of the ridge consists of 10 first-order spreading segments (N1-N10), the Valdivia Fracture Zone consists of five first-order segments (V1-V5), and the southern section of the ridge consists of five surveyed first-order segments (S1-S5). Segments N9 and S5 are each broken into two second-order segments (N9N-N9S and S5N-S5S) by nontransform offsets (Figure 1). We analyze the longest segments in each section where data coverage and quality are highest, while avoiding segments where faulting is irregular and complex. Hence, we focus on segments N1, N5, N8, N9N, N9S, N10, V4, S5N, and S5S.
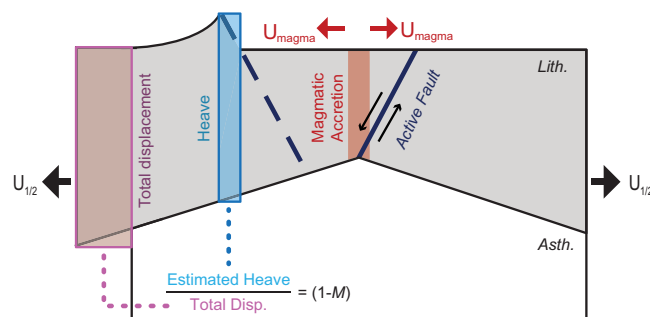

Figure 2. Illustration of magmatic and tectonic extension. Oceanic lithosphere (grey) is spreading at a half spreading rate $U_{1/2}$. Magmatism (light red) at the ridge axis accommodates a fraction $M = U_{magma}/U_{1/2}$ of the total spreading. Faults form near the ridge axis and then migrate away from the axis into thicker, stronger lithosphere. They eventually become inactive (dashed line) once the energy required to keep them slipping exceeds that needed to create a new fault (bold line) closer to the ridge axis. The accumulated heave (blue box) on the faults, accommodates a fraction $(1 - M)$ of the total spreading (purple box).

3. Methods

3.1. Measurements of Fault Characteristics

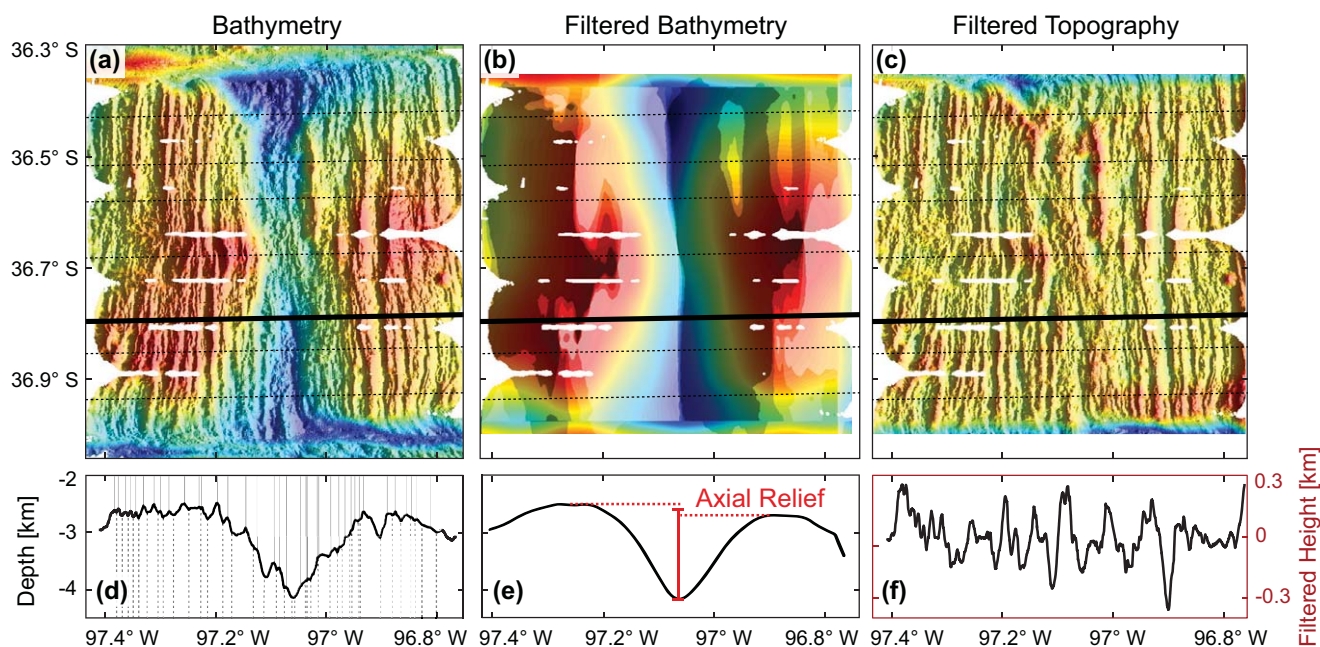We used SeaBeam 2000 multibeam bathymetry data collected during research cruise PANR04MV in January–

Figure 3. Shaded relief maps of segment N1 (a) multibeam bathymetry, (b) low-pass filtered bathymetry with wave numbers $> (2\pi/20)$ km^{-1} (or wavelengths < 20 km) removed, and (c) the high-pass filtered map found by subtracting the low-pass bathymetry from the raw bathymetry. Lines show transects along which faults were identified and axial relief was measured. Profiles of (d) depth, (e) low-pass filtered depth, and (f) high-pass filtered topography along the bold transect in Figures 3a–3c; the black depth scale applies to Figures 3d and 3e, while the red filtered height scale applies to Figure 3f. The high-pass filtered bathymetry was used to pick fault tops and bottoms, marked with thin solid and dashed lines, respectively, on the unfiltered bathymetric profile (Figure 3d). The red bar in Figure 3e shows axial relief, derived from the low-pass filtered bathymetry (see text).

March 1998 aboard the R/V Melville [*Karsten et al.*, 1999]. To quantify fault characteristics, the data were first gridded at 100 m × 100 m. We then applied a high-pass Fourier filter that isolated wavelengths ≤ 20 km to distinguish the short-wavelength structure of individual faults from the longer-wavelength morphology of the axial valley ridge (Figures 3a–3c). Three grids were subsequently used in our analysis: the original unfiltered bathymetry, the filtered bathymetry containing the short wavelengths, and the filtered bathymetry containing the long-wavelengths. For each grid, we examined individual transects along spreading flow lines determined from the relevant opening pole of *Tebbens et al.* [1997] (Figures 3d–3f). Between 3 and 18 transects were defined for each segment. When possible, we selected transect locations within the well-resolved parts of the multibeam swaths (i.e., away from swath edges) to sample seafloor uniformly along each segment while capturing topography near both segment ends and segment centers. This resulted in transect spacings of 3–15 km.

To identify individual faults, we examined maps of the unfiltered bathymetry, the short-wavelength bathymetry, its gradient and curvature, and profiles of these maps taken along the individual transects (Figure 4). Two thousand one hundred fifty-seven faults were identified as continuous, linear features that terminate or branch at both ends, distinguished from volcanic features with rounded margins and no clear termini (Figure 4a). The continuous, high-slope scarp faces were accentuated in maps of filtered bathymetry gradient (Figure 4b). Faults appeared in maps of filtered bathymetry curvature (Figure 4c) as long, linear bands, marking the high-curvature break in slope at the top and bottom of fault scarps. Volcanic and hummocky material appeared in maps of curvature as pseudocircular closed loops, marking the break in slope at the top and bottom of cones and hill-like fabrics.

After the faults were identified, we used the original unfiltered bathymetry to pick the shallowest parts of the fault as scarp tops and the deepest level of the basins as scarp bottoms along the transects (Figures 4e–4g). These picks were used to estimate the original, undegraded throw of the fault. Estimates of the least-degraded, original fault dip were obtained by selecting the most continuous, high-angle face of each scarp. The mean spacing of faults along each transect was computed by dividing the distance between the westernmost and easternmost fault scarp tops by the total number of faults crossed.

To verify our measurements, we examined the frequency distribution of fault throws. Natural fault populations are predicted to display an exponential frequency distribution for faults having lengths comparable to
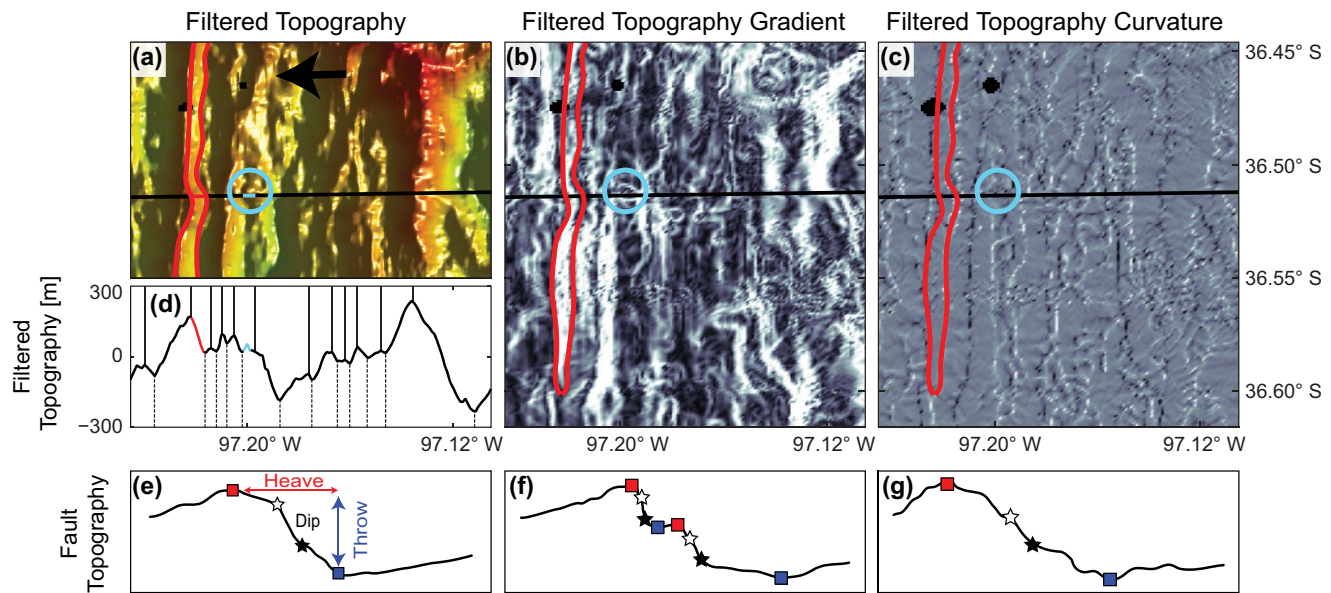
Figure 4. Imagery used to distinguish faults (bold red lines) from volcanic/hummocky topography (bold light-blue circles) for segment N1 include shaded relief maps of (a) filtered bathymetry (black arrow shows spreading direction), (b) gradient, and (c) curvature of the high-pass (containing short wavelengths) filtered bathymetry. The black line indicates an example flow line transect along which the profile of (d) filtered bathymetry was taken. In Figure 4d, picks of fault tops and bottoms are marked by solid and dashed lines, respectively; red and light-blue sections show the highlighted fault and cone in Figures 4a–4c. (e–g) Example profiles of faults are shown with picks used to measure fault throw, marked by red and blue squares, and to estimate fault scarp dip, marked by white and black stars. Examples include (e) a profile with a clear fault top, bottom, and scarp face, (f) two terraced faults, and (g) a profile that is more difficult to interpret due to a highly degraded fault scarp.

or greater than the brittle layer thickness [*Carbotte and Macdonald*, 1994; *Cowie et al.*, 1993], and exponential distributions in scarp heights and fault spacing have indeed been observed at the East Pacific Rise [*Bohnenstiehl and Kleinrock*, 1999; *Bohnsenstiehl and Carbotte*, 2001]. Consistent with these studies, the observed distribution of fault throws (Figure 5a) shows little deviation from exponential behavior, confirming that we identified a representative fault population without the picking process or limited data resolution obscuring all of the smaller faults. Methodological and natural biases lead to problems in estimating the dips of active faults, and are discussed below in section 4.1.

3.2. Measurements of *M*, Axial Relief, Segment Length, and Offset Distance

To characterize relationships between tectonomagmatic variables, axial morphology, and ridge geometry, we estimated the fraction of extension taken up as slip on normal faults, $(1 - M)$, and attributed the remaining fraction, M, primarily to extension accommodated by the accretion of new crust. A value of $M = 1$ would correspond to completely magmatic spreading with no faults, while $M = 0$ would correspond to completely amagmatic spreading accommodated entirely by fault slip. Estimating M required measurements of the cumulative horizontal displacement of the faults as a function of distance from the axis. Unfortunately, the degradation of bathymetry by erosion and mass wasting prohibited accurate measurements of the heave and dip of the original fault surface. Therefore, following *Escartín et al.* [1999], we estimated heave using the present-day throw, the observable least impacted by erosion and mass wasting, and an average dip for an active fault of 45°, which we justify below in section 4.1. We next calculated $(1 - M)$ for each transect by measuring the cumulative heave between the westernmost and easternmost faults and dividing by the total distance between them (Figure 2). This method produces values of mean $(1 - M)$ nearly identical to those obtained with the approach of *Escartín et al.* [1999], who find the best fit slope of cumulative heave varying with distance to the ridge axis. The standard deviation in $(1 - M)$ is estimated from the variation in the best fit slope of cumulative heave versus across-axis distance within 10 km wide windows along each transect.

To characterize axial morphology, we measured the relief of the axial valley as the difference in depth between the deepest part of the valley and the mean depth of the shallowest peaks flanking the valley along transects of the filtered bathymetry containing the long-wavelengths (Figure 3e). We also measured the length of each ridge segment as the distance along axis between first-order and second-order segment
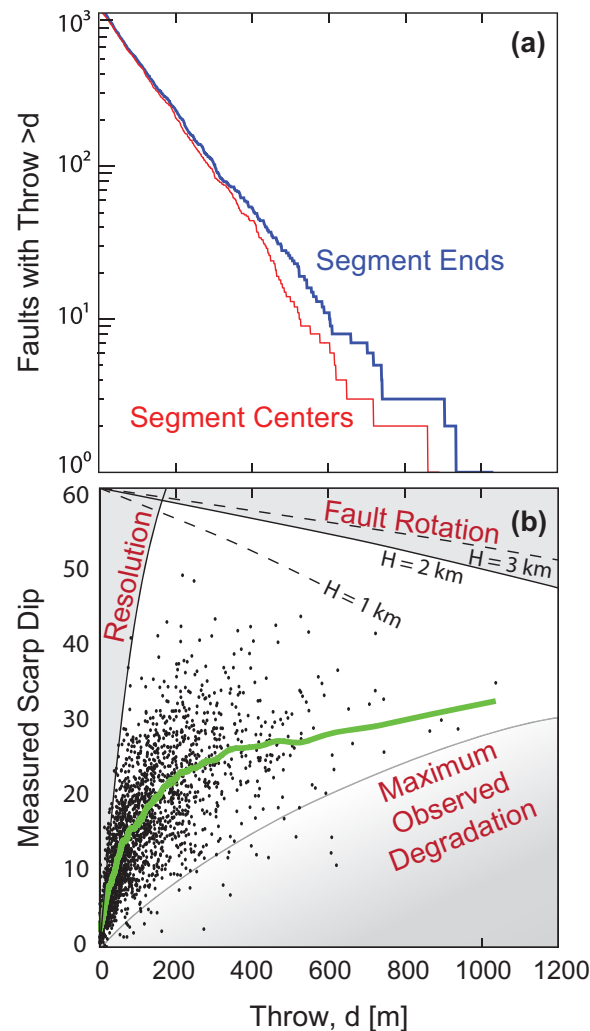
Figure 5. (a) Cumulative frequency distribution of fault throws for faults nearer to segment offsets than segment centers (blue line) and nearer to segment centers than segment offsets (red line). The nearly straight lines in these plots indicate approximately exponential distributions, which is predicted for a population of faults having lengths comparable to or greater than the brittle layer thickness [*Carbotte and Macdonald*, 1994; *Cowie et al.*, 1993]. (b) Measured fault dip (dots) and median measured fault dip (green line) versus throw. Curve marked "Resolution" shows the predicted maximum angles that can be resolved by the 100 m gridding of the bathymetry data. Curve marked "Fault Rotation" is the predicted rotation of an individual fault scarp with increasing throw in a H = 2 km thick (solid line) elasto-plastic plate overlaying a viscous asthenosphere [*Olive and Behn*, 2014]. Dashed lines show models with H = 1 and H = 3 km, illustrating that scarp rotation rate scales with 1/H. The lowermost curve was sketched by eye to mark the approximate trend of an increase in the minimum angles with throw.

offsets, and the distance of each offset as the distance between first-order or second-order spreading segments.

3.3. Quantifying Correlations Between Measurements

We tested for relationships between observables in several ways. First, we tested for correlations between transect means of axial relief, M, fault throw, fault spacing, and the along-axis distance to the nearest segment end. A total of $n = 57$ transects were used. To examine the effect of (first-order and second-order) offset distance, we tested for correlations between offset distance between adjacent segments and the means of axial relief, M, fault throw, and fault spacing within different groups of transects. Four of the groups were defined based on bins of the proximity, d, of each transect to the nearest segment end: $d \leq 10$ km ($n = 16$), $10 < d \leq 20$ km ($n = 15$), $20 < d \leq 30$ km ($n = 14$), $d > 30$ km ($n = 12$). A fifth grouping ($n = 18$) was done by separating transects within the northern and southern half of each segment. Further, we tested for correlations between segment length and the segment mean ($n = 9$ segments) of all fault parameters.

Correlations were quantified using Spearman's rank correlation coefficient. Although Pearson's product-moment correlation coefficient is more widely used in the geologic literature, it only detects linear correlations. Spearman's rank correlation is more general; it detects any monotonic relationship, linear or curved, and is less sensitive to outliers. We also computed a "p value" for each correlation, which gives the probability that the computed correlation coefficient, or larger, occurs by random sampling from a population with a true correlation of zero. The p value depends on the size of the sample being considered. For correlations between axial valley relief, fault characteristics, and along-axis distance, we computed $n = 57$

individual transect means. For correlations of axial relief and fault characteristics with the nearest ridge offset distance, we computed $n = 12 - 16$ means for the four transect bins of proximity d to the offset, and $n = 18$ means for the fifth transect grouping based on the north-half versus south-half division of each segment. For correlations of axial relief and fault characteristics with segment length, we computed $n = 9$ segment means. Low p values indicate a small probability of the true correlation being zero. We considered p values less than 0.05 to indicate a significant correlation.

We also tested for differences between the measured properties at segment inside corners (seafloor on the transform-fault side of the ridge segment) and outside corners (seafloor on the fracture zone side of the

ridge segment) by dividing each segment into equal-area quadrants. East and west sides were separated at the ridge axis, and these half-segments were sectioned into northern and southern groups by the midpoint between segment ends. We tested for differences in the mean values of M, fault spacing, fault throw, and axial relief between the inside and outside corner groups using the nonparametric Mann-Whitney U-test. This test determines the probability that incomplete sampling of a single population yields different sample means, even though the true means are identical.

3.4. Comparisons With Geochemical Proxies of Extent of Partial Melting and Crystallization

To explore whether variations in the supply of magma to the ridge axis or the crustal magma plumbing system might influence the amount of extension accommodated on faults measured at the surface, we qualitatively compared estimates of M with geochemical indicators of the extent of partial melting from the analyses of *Milman* [2002]. We examine two geochemical proxies recorded in seafloor basalts: (1) the mean degree of melting, F, as inferred from $[Na_2O]_8$ and $[CaO]_8/[Al_2O_3]_8$ (estimated concentrations at 8 wt % MgO using regression), and (2) MgO content, which generally decreases with increasing extent of fractional crystallization in magma storage zones in the crust. Values of F and MgO content were smoothed along axis to aid in the visual comparison between geochemical data and M using a 2 km running-average filter.

4. Results

4.1. Relations Between Measured Fault Dip and Throw

Examining how measured scarp dip varies with throw reveals information about fault growth and rotation, and topographic degradation by erosion and mass wasting (Figure 5b). Measured scarp dips span a wide range of values at a given throw, and the envelope encompassing the range of scarp dips narrows with increasing fault throw. One boundary of this envelope occurs at the smallest throws, where the maximum observed dip increases sharply from $<5°$ up to $\sim50°$ as throw increases from 0 to ~200 m. This boundary is readily explained by data resolution limits: the maximum observable dip is given by the arctangent of the throw divided by the horizontal resolution of the multibeam data, which is ~100 m. The envelope boundary of maximum fault dips for faults with throws >200 m can be explained by rotation of the active fault with increasing slip, consistent with predictions of numerical models, and analytic scaling laws for faulting of an elasto-plastic lithosphere overlying a low-viscosity asthenosphere [*Olive and Behn*, 2014]. The boundary shown is from such a model with an effective elastic plate thickness of 2 km. Indeed, the observed variation in maximum fault dip as a function of throw decreases from nearly $50°$ at throws of ~300 m to $\sim35°$ at throws >1 km, but fails to reach the higher predicted dips, presumably due to degradation of the fault scarps. Finally, we attribute the lower envelope boundary to be the maximum extent that mass wasting and erosion can reduce the apparent fault dip. The decreasing influence of erosion and mass wasting on fault dip with increasing topographic wavelength over a given time span is consistent with diffusive erosion models [e.g., *Webb and Jordan*, 2001].

In summary, fault rotation and fault scarp degradation introduce significant complexity into the estimation of original fault dip, which is in turn needed to quantify fault heave and M as described in section 3.1. In our preliminary treatments, we consider mean dips of $30°$, $45°$, and $60°$, and dips that varied with slip as predicted by the elasto-plastic faulting models of *Olive and Behn* [2014]. All cases produced similar trends despite subtle differences in mean values of M (M scales with the tangent of fault dip, so an assumed dip of $30°$ reduces mean M by 11%, while a dip of $60°$ increases M by 4%). Additionally, the case where dip decreased with increasing throw slightly strengthened the significance of the reported correlations. Conservatively, we therefore report only the results for a constant mean dip of $45°$ because it is comparable to the maximum measured dips.

4.2. Observations of Individual Segments
4.2.1. Segment N1

The northernmost segment of the Chile Ridge, N1 (Figure 6a), is a 70 km long first-order spreading segment bounded in the north by a ~1000 km long transform fault zone, and in the south by en echelon transform faults and intra-transform spreading centers (ISCs) that offset N1 east of segment N5 by ~250 km. Segment N1 exhibits an "hourglass" morphology, defined by depth contours running along the spreading axis that widen near the segment ends as the axial valley deepens and narrow toward the segment center as the
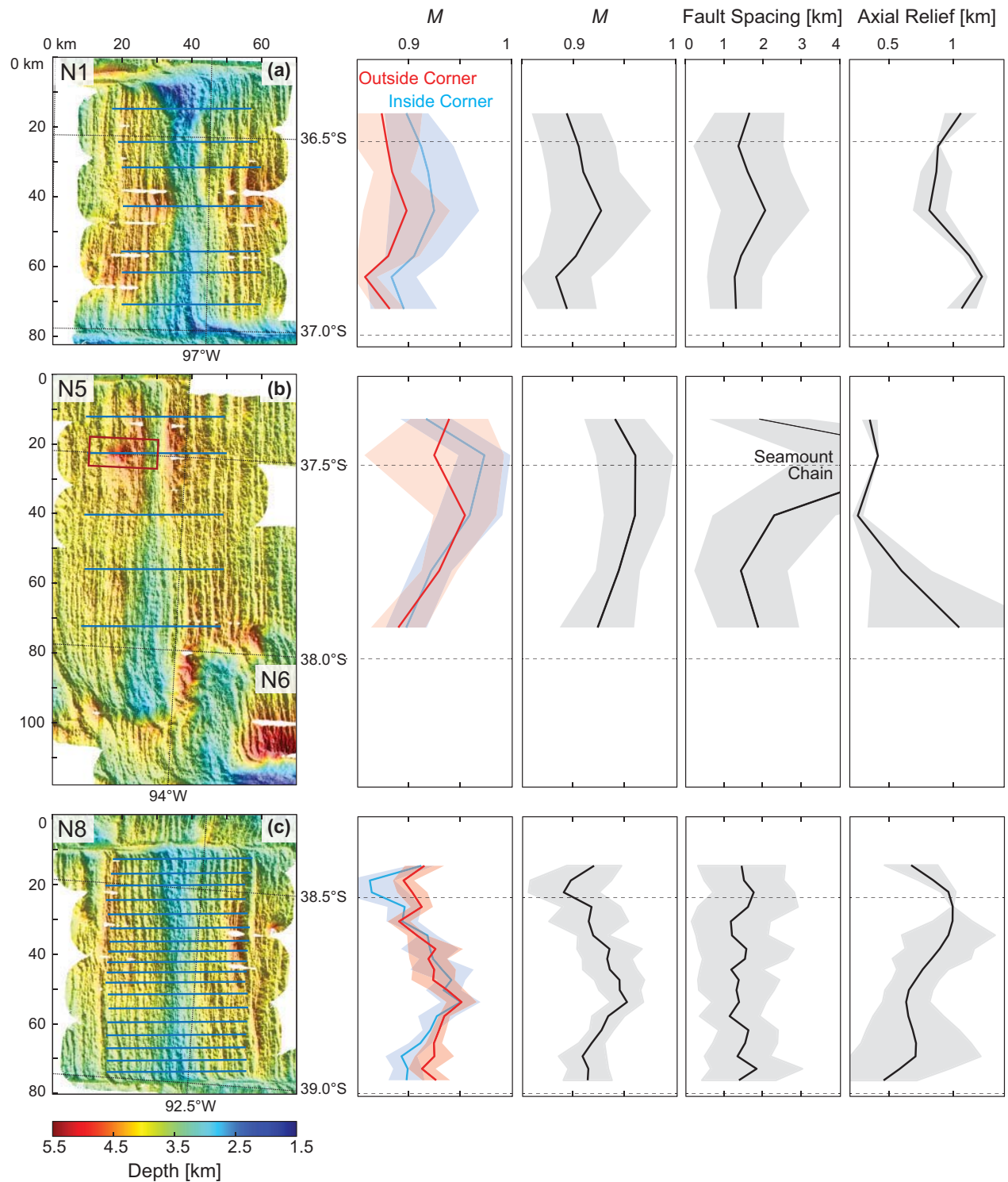
Figure 6. Chile Ridge bathymetry maps of studied segments (a) N1, (b) N5, (c) N8, (d) N9N, N9S, (e) N10, (f) V5, and (g) S5N, S5S, showing transects taken along spreading flow lines (blue lines) used to identify and measure faults, and to calculate axial relief. From left to right, the accompanying columns are: estimates of mean M (lines) and one standard deviation (colored backgrounds) for transect halves grouped by proximity to outside (red) and inside (blue) corners, estimates of total mean M, mean fault spacing, and axial relief (black lines) with one standard deviation (grey background) for whole transects.

valley shoals. The axial valley is asymmetric across the axis near segment ends, deepening more toward the inside corner side of the ridge. Seafloor fabric on both sides of the axial valley is dominated by large, ridge-parallel abyssal hills composed of normal fault complexes that run nearly half the segment length. As shown
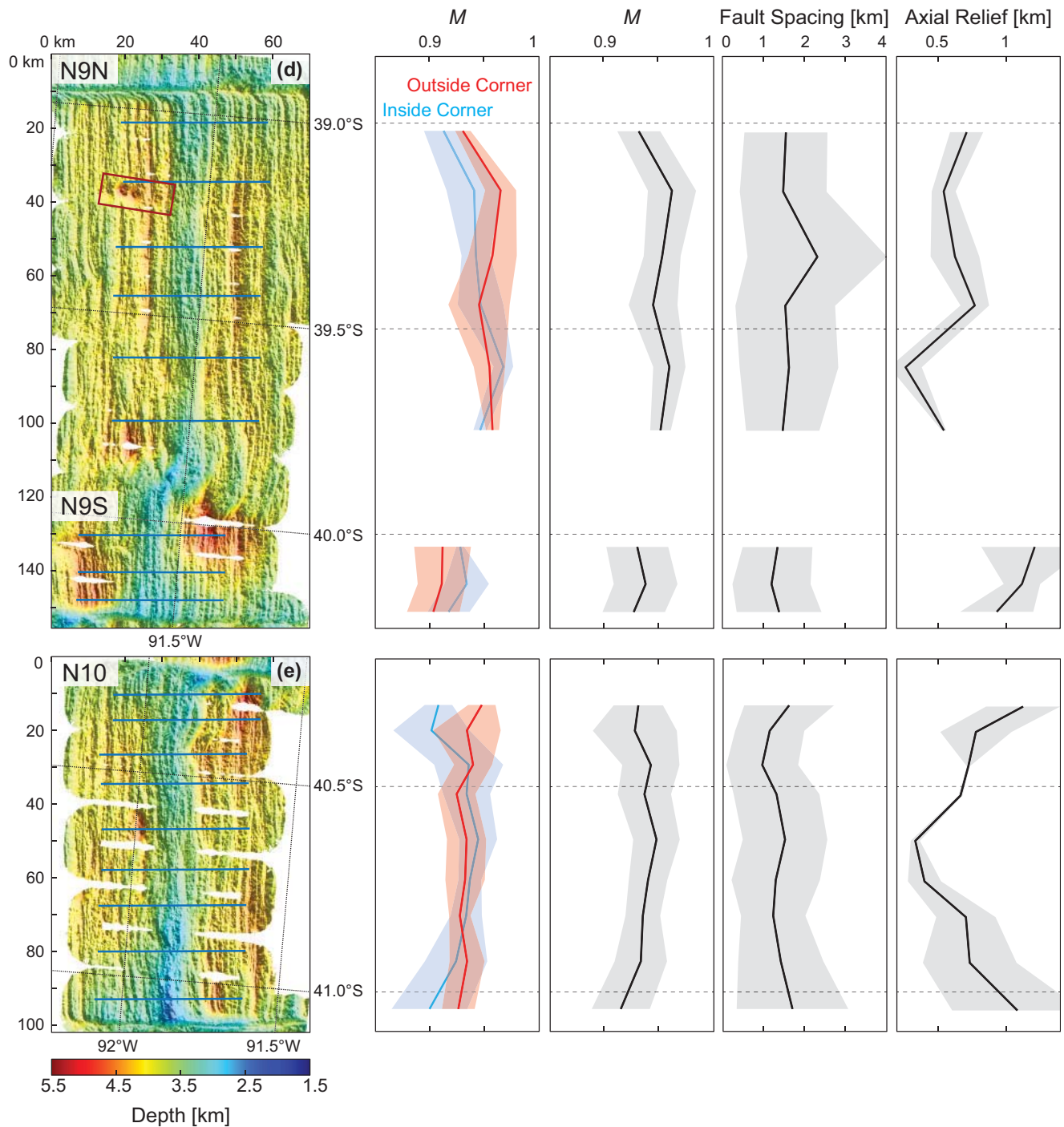
Figure 6. (continued)

in Figure 3, these abyssal hills are superimposed on the long-wavelength axial valley topography and tend not to strike parallel to the curving axial valley flanks, but rather initiate at a consistent distance from the axis of approximate east-west symmetry.

Variations in a number of other key observables are seen along the ridge segment. From the segment ends toward the segment center, the relief of the axial valley decreases from >1 to ~0.75 km. The reduction in relief is ~0.1 km more pronounced from the southern segment boundary in response to shallow flank bathymetry on the west side of the ridge axis. As relief decreases from the segment ends to the segment

Figure 6. (continued)

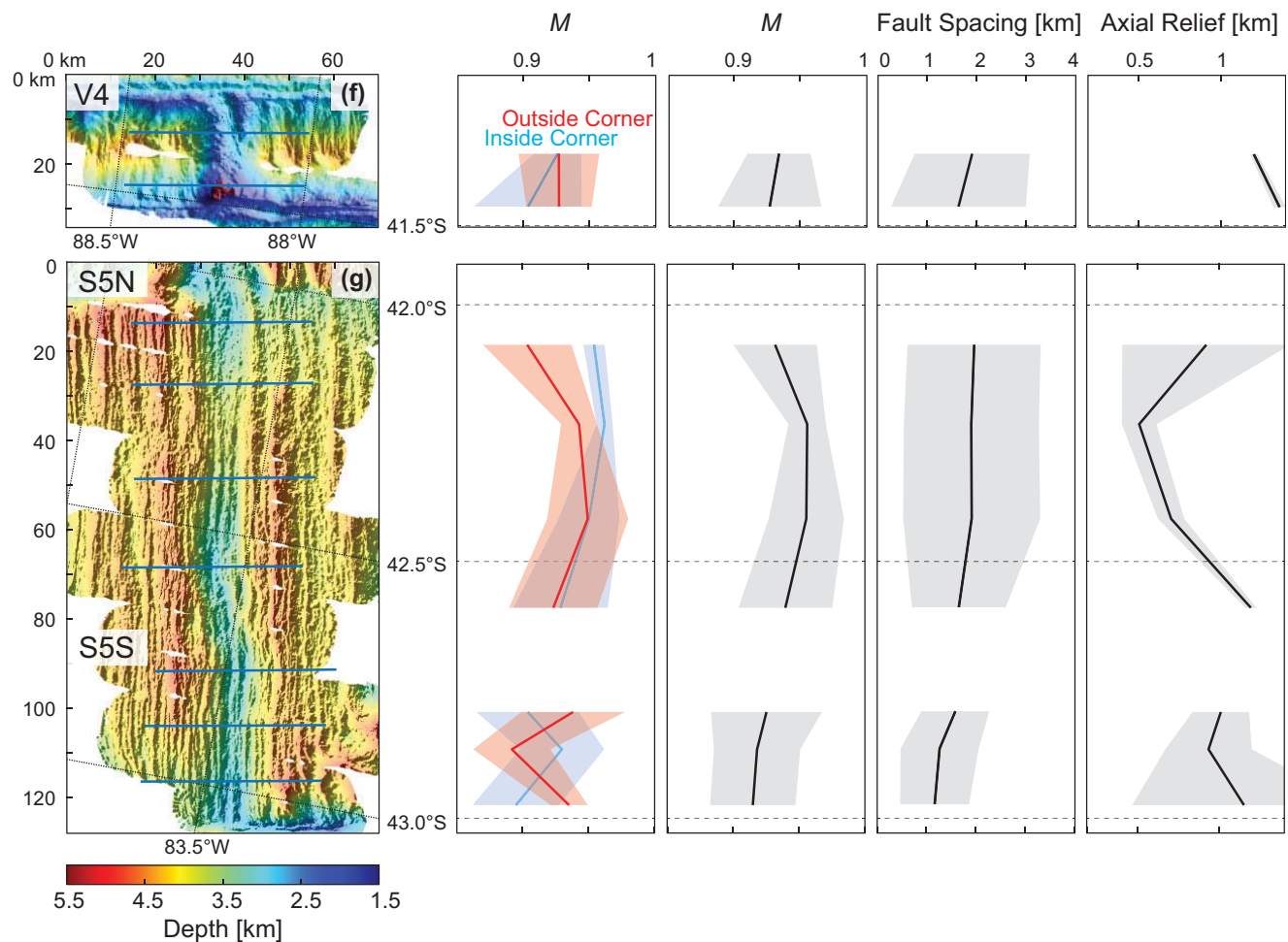center, fault spacing increases from ~1.5 to ~2 km and M increases from 0.88 to 0.92. This trend in M is seen at both outside and inside corners, but M on inside corners is overall greater by approximately one standard deviation.

4.2.2. Segment N5

Segment N5 is a 95 km long first-order spreading segment that is offset ~250 km east of segment N1 (Figure 6b). It is bounded in the south by pseudofaults associated with the dueling propagation between the southern end of N5 and northern end of N6, which is offset ~20 km east. Segment N5 exhibits an asymmetric hourglass morphology. The narrowest "waist" of the hourglass and shallowest part of the ridge axis occur near a short chain of volcanic cones, ~25 km south of the northern segment boundary and ~70 km north of the southern boundary. To the south, the relief of the axial valley (1 km) is substantially greater than in the north (~0.3 km). From the segment ends to the shallowest part of the ridge, fault spacing increases from ~1.5 km to >4 km, and M increases from ~0.92 to 0.96. This trend in M is similar between the outside and inside corners, except near the seamount chain, where $M = 0.97$ on the inside corner (seamount side) and $M = 0.93$ on the opposite side.

One obvious feature influencing the morphology of segment N5 is the competing spreading segment N6. Segment lengthening and shortening is recorded in the seafloor fabric west of the southern terminus of segment N5, resulting in bathymetric ridges that tend to strike southward and curve toward segment N6. We therefore picked transects away from this complex fabric, and chose not to analyze segment N6.

4.2.3. Segment N8

Segment N8 is a 65 km long first-order spreading segment (Figure 6c), bounded in the north by a transform fault extending from the ISC N7 and in the south by a transform fault that offsets segment N9 80 km to the
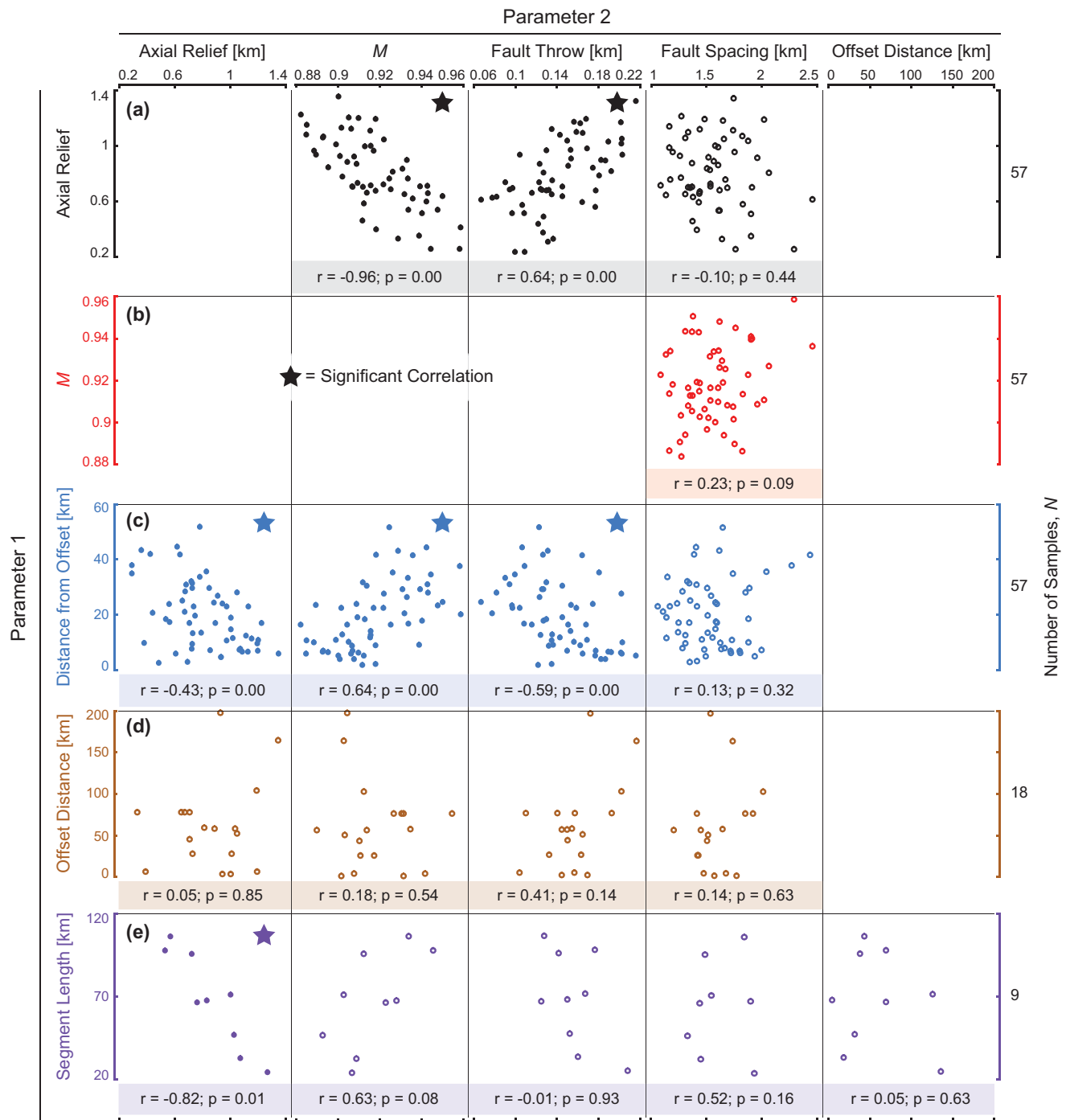
Figure 7. Plots showing correlations of (a) axial relief, (b) *M*, (c) distance of the transect from the nearest offset, (d) segment offset distance, and (e) segment length with each measured parameter. Color shaded boxes contain Spearman's rank correlation coefficient, *r*, and a *p* value. The *p* value is the probability that a correlation as strong as or stronger than measured would result from a distribution with no correlation through random change and incomplete sampling of the data. We consider a *p* value less than 0.05 to be significant. Significantly correlated pairs have filled symbols and are marked by a star.

east. Segment N8 exhibits a more subdued hourglass morphology than N1 or N5, primarily because the segment center is deeper. Like other segments on the Chile Ridge, the axial relief shows a local minimum (~0.6 km) at the shallowest part of the segment. However, unlike the other segments, the relief lessens very close to the segment ends where the axial valley flanks deepen toward the transform offset more rapidly than the axial valley. Fault spacing displays no long-wavelength change along the segment, whereas *M* increases toward the shallowest part of the segment with an overall variation from 0.85–0.95. Inside corner
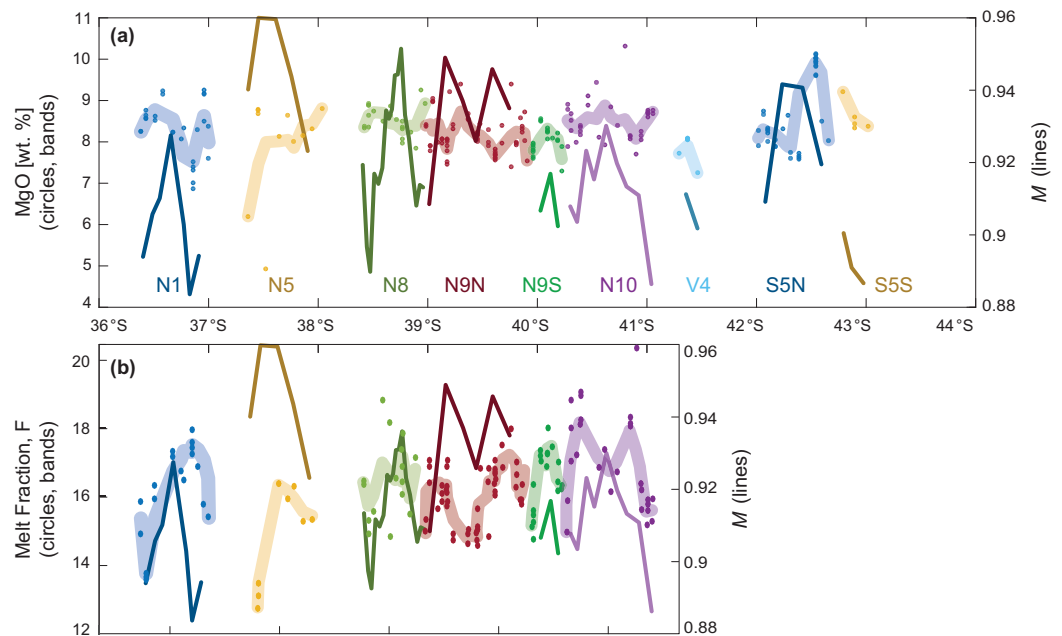
Figure 8. Estimated values of (a) MgO content of seafloor basalts and (b) extent of partial melting (in %, colored circles [*Milman*, 2002]), and values smoothed with a 2 km moving-average window (shaded and colored bands) are shown alongside estimates of M (colored lines) for each of the studied segments where geochemical analyses were available.

values of M tend to be lower than outside corners values near the segment ends, but show no difference near the segment center.

4.2.4. Segment N9

Segment N9, the longest segment in the study area, is a 140 km long first-order spreading segment that is broken into two second-order segments, N9N and N9S, by a nontransform offset (NTO) (Figure 6d). N9 is bounded in the north by a transform that offsets it 80 km east of segment N8 and in the south by a transform that offsets it 25 km east of segment N10.

Second-order segment N9N is 110 km long and bounded in the south by a NTO that offsets it 8 km east of N9S. Unlike other segments studied, segment N9N exhibits a morphology resembling two "stacked" hourglasses. A deep, wide axial valley at the northern transform boundary narrows and shoals for ∼30 km to the south, where a volcano chain similar to that seen at N5 strikes west from the axis. The valley then deepens and widens for another ∼20 km southward. This pattern of narrowing and widening then repeats once more before reaching the NTO. Axial relief varies accordingly: it is locally small near the two narrow hourglass waists (minimum 0.5 km in the north and 0.25 km in the south) and locally large between the waists and near the segment ends (0.7 km in the north, 0.8 km in the center, and 0.55 km in the south). M varies in a correlated, but opposite manner: it is locally high near the hourglass waists (minima in axial relief) and smaller between the waists and near the segment ends. Thus, N9N exhibits a wavelength of variation in morphology that is distinct from that of tectonic segmentation.

Second-order segment N9S is 30 km long and exhibits a semihourglass morphology evident in the widening of depth contours near the southern segment boundary. Valley flanks on the inside corners of both the NTO in the north and the transform in the south are anomalously shallow. There is a slight southward decrease in axial relief from 1.3 to 0.9 km. Fault spacing tends to decrease from ∼1.5 km at the segment ends to ∼1 km at the segment center. The variations in mean M along the segment are small compared to the standard deviation.

4.2.5. Segment N10

Segment N10 is a 95 km long first-order spreading segment (Figure 6e), bounded in the north by a transform fault that offsets it ∼25 km west of segment N9 and in the south by the Valdivia Fracture Zone: a 600 km wide east-west trending regime of en echelon ISCs offset by long transform faults (Figure 1). Segment N10 exhibits hourglass morphology, although the strike of the ridge axis varies, making it less linear
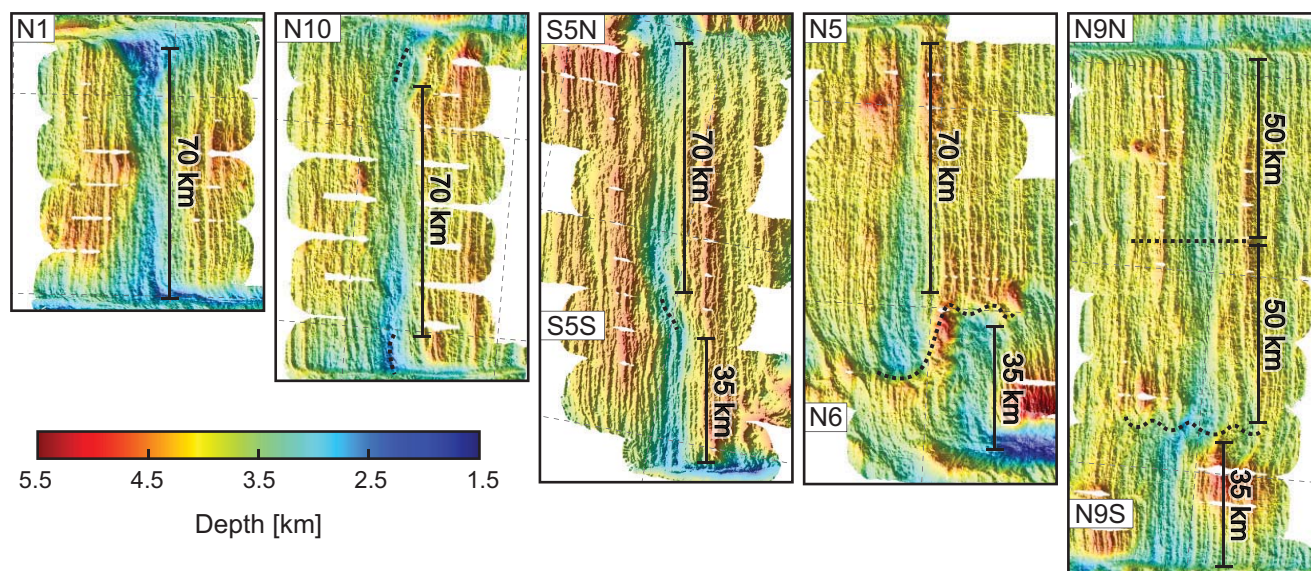
Figure 9. Seafloor bathymetry maps of five studied segments. Black bars follow straight, hourglass-like portions of the ridge axis to indicate magmatic segmentation, and dashed lines show magmatic segment boundaries. As the distance between transform offsets lenghtens, the axial valley deviates from linear strike, leading to nontransform offsets and traditional tectonic segmentation of the ridge axis.

than many of the other segments. Similar to the trends observed along other segments, there is a decrease in relief from >1.0 to 0.2 km away from the segment ends toward the segment center. Fault spacing shows little variation, while *M* is highest (0.95) near the segment center. From the southern segment boundary, *M* increases toward the segment center by an amount that is comparable to the standard deviation. Near both segment ends, *M* is lower on the inside corners than on the outside corners.

4.2.6. Segment V4

Segment V4 is a 20 km long first-order intra-transform spreading center in the Valdivia Fracture Zone, bounded in the north and south by long transform fault segments that offset it from neighboring ISCs (Figure 5f). The segment is tectonically dominated by large-slip faults, with an axial valley that is split by a ridge

Table 1a. Correlations of measured and estimated parameters: Spearman's Rank Correlation Coefficient, *p* Value, and Sample Size for Each Pair of Measured Parameters, Computed Separately for the Whole Ridge, and for Inside and Outside Corners[a]

| Parameter 1 | Parameter 2 | Whole Ridge | | Outside Corner | | Inside Corner | | Corr. Comparison Significance Test | Sample Size |
		Corr. Coeff.	p Value	Corr. Coeff.	p Value	Corr. Coeff.	p Value	p Value	
M	Spacing	+ 0.23	0.09	+ 0.24	0.07	+ 0.18	0.19		57
Axial Relief	M	− 0.96	0.00	− 0.70	0.00	− 0.67	0.00	0.38	
	Throw	+ 0.64	0.00	+ 0.65	0.00	+ 0.55	0.00	0.21	
	Spacing	− 0.10	0.44	− 0.10	0.46	− 0.02	0.89		
Distance from Offset	Axial Relief	− 0.43	0.00	− 0.30	0.02	− 0.44	0.00	0.20	
	M	+ 0.64	0.00	+ 0.39	0.00	+ 0.64	0.00	0.04	
	Throw	− 0.59	0.00	− 0.34	0.01	− 0.65	0.00	0.01	
	Spacing	+ 0.13	0.32	+ 0.00	0.98	+ 0.08	0.54		
Offset Distance	Axial Relief	+ 0.05	0.85	+ 0.31	0.27	+ 0.05	0.86		18
	M	+ 0.18	0.54	− 0.06	0.83	− 0.14	0.64		
	Throw	+ 0.41	0.14	+ 0.31	0.28	+ 0.19	0.53		
	Spacing	+ 0.14	0.63	+ 0.25	0.39	+ 0.36	0.21		
Segment Length	Axial Relief	− 0.82	0.01	− 0.78	0.02	− 0.82	0.01	0.28	9
	M	+ 0.63	0.08	+ 0.53	0.15	+ 0.57	0.12		
	Throw	− 0.01	0.93	− 0.67	0.06	− 0.67	0.06		
	Fault Spacing	+ 0.52	0.16	+ 0.00	1.00	+ 0.33	0.39		
	Offset Distance	+ 0.05	0.63	− 0.02	0.94	− 0.02	0.94		

[a]The *p* value is the probability that random chance and incomplete sampling of the data lead to correlation coefficients as large as or larger than those measured when sampling from a total population having a true correlation coefficient of zero. A correlation comparison significance test utilizing the Fisher *r-to-z* transformation was used to produce a second *p* value; this value is the probability that the true correlation coefficients associated with inside and outside corners are equal, but appear different due to incomplete sampling and random chance. Significantly correlated pairs are highlighted.

Table 1b. Correlations of Measured and Estimated Parameters: Comparison of Mean Values for M, Fault Spacing, Fault Throw, and Axial Relief at Outside and Inside Corners[a]

	Outside Corner		Inside Corner		
Parameter	Mean	Std.	Mean	Std.	Mann-Whitney U-test p *Value*
M	0.92	0.02	0.92	0.02	0.63
Spacing *(km)*	1.61	0.39	1.65	0.43	0.70
Throw *(km)*	0.13	0.12	0.13	0.13	0.83
Axial Relief *(km)*	0.79	0.30	0.80	0.29	0.59

[a]The nonparametric Mann-Whitney U-test was used to determine the probability that the differing measured means arise even though the true means associated with the outside and inside corners are identical. In all cases, we consider a p value less than 0.05 to be significant.

in the north and deepens significantly in the south. The transform fault fabric and short segment length limited fault measurements to only two transects.

Axial relief is greatest in the south where the axial valley is deepest, increasing from 1.2 to 1.5 km from north to south, the highest relief of any measured transect. This corresponds to a decrease in fault spacing from 2.0 to 1.4 km. Like the other segments studied, M decreases as relief increases, here from 0.93 to 0.92, though this variability is well within the standard deviation on M. Estimates of M for both inside and outside corners are ∼0.93 in the north; inside corner values decrease to 0.9 in the south while outside corner values remain at 0.93.

4.2.7. Segment S5
Segment S5, the southernmost surveyed and studied segment, is a 115 km long first-order spreading segment that is broken into two second-order segments, S5N and S5S, by a slight eastward jog in the axial valley (Figure 6g). S5 is bounded in the north by a Valdivia Fracture Zone transform fault, and in the south by a transform fault that offsets the next segment ∼60 km to the east.

Second-order segment S5N is 70 km long and exhibits an hourglass morphology. The northern inside corner is anomalously shallow and the northern outside corner is anomalously deep. Like many of the other segments, axial relief tends to decreases from the segment offsets toward the segment center (here from >1 to 0.5 km), while M increases from the offsets toward the segment center (from 0.92 to 0.96). M at the inside corner is 0.05 greater than at outside corner in the north, and approximately equal in the south. There is no apparent systematic variation in fault spacing.

Second-order segment S5S is ∼45 km long and exhibits a subdued hourglass morphology. The inside corner of the southern section is shallower than the opposite outside corner. Axial relief decreases from >1 km near the segment offsets to ∼0.8 km near the segment center. From north to south, fault spacing decreases from 1.6 to 1.1 km, and M decreases from 0.93 to 0.92, although this variation in mean M is small compared to the standard deviation. Compared to the outside corners, M at the inside corners is higher near the segment center and lower near the segment ends.

4.3. Intrasegment Correlations of Transect Means
Using the observations made at these nine Chile Ridge segments, we now examine correlations between faulting, morphological characteristics, and M to illuminate the relationships governing segment-scale and along-axis variations (Figure 7, rows a and b). We find that axial relief correlates significantly with M and fault throw (from which estimates of M are partially derived), demonstrating a close relationship between the longer-wavelength axial morphology and magmatic extension along these segments. However, while M and axial relief correlate strongly, neither variable shows a significant correlation with fault spacing. Thus along-axis changes in M are accommodated by changes in slip along faults without a strong change in fault spacing.

To explore the influence of segment boundaries, we compute correlations between the distance from the nearest segment end along the ridge axis, axial relief, M, and fault characteristics (Figure 7, row c). We find that as distance from the segment end increases, axial relief and fault throw tend to decrease, while M tends to increase. This finding is consistent with global trends of shallower axial valleys being associated with greater values of M [*Ito and Behn*, 2008] and mantle magma supply to the ridge axis [*Dunn et al.*, 2005; *Lin and Phipps Morgan*, 1992].

4.4. Intrasegment Evidence for Magmatic Segmentation

Magmatic segmentation refers to the spatial separation of magma delivery and plumbing systems at a ridge axis [*Carbotte et al.*, 2015]. In this paper, we use along-axis variations in M, axial valley relief, and petrologic indicators as proxies for magmatic segmentation.

First, we compare along-axis variations in M to the MgO content of seafloor basalts *Milman* [2002] (Figure 8a). Variations in M and MgO appear to be positively correlated at some segments, negatively correlated in others, and in some locations are out of phase or entirely lack any correlated variation. Thus, there appears to be no systematic relation between the amount of magmatic extension and the processes of magma storage and cooling (i.e., crystallization) in the crust reflected by the MgO content.

We next compare along-axis variations in M to estimates of the extent of partial melting of the mantle, F, *Milman* [2002] (Figure 8b). In all but one segment (N10), F tends to be locally low where M is locally low (usually near segment ends) and F tends to be locally high where M is locally high (usually near segment centers). Along segment N9N, two distinct local maxima in F and M within the second-order segment are separated by a local minimum in both quantities. These findings suggest that local highs in melt supply, inferred from the geochemistry data, contribute to local highs in magmatic extension (and lows in tectonic extension), and that variations in the two demarcate a scale of magmatic segmentation of approximately 50 ± 20 km.

A closer look at the bathymetry in map view offers further insight (Figure 9). Segments shorter than or comparable to the 50 ± 20 km wavelength of magmatic segmentation (e.g., N1) exhibit relatively straight axial valleys with north-south symmetry and single maxima in M and F. Segments with lengths greater than the observed scale of magmatic segmentation display subtle jogs in the axial valley (e.g., N10) or multiple maxima in M and F (e.g., N9N). Segments that are much longer than 50 ± 20 km exhibit prominent axial jogs and second-order segment offsets that correspond to distinct magmatic segments seen in M and F (e.g., N5/N6, N9, and S5). Thus, we infer that the length scale of magmatic segmentation of 50 ± 20 km is at least partially decoupled from the length scale of tectonic segmentation.

4.5. Comparisons of Inside and Outside Corners

We examine the effect of transforms on the cross-axis symmetry of the seafloor structure by computing correlations for inside and outside corners separately (Table 1a). Parameter means for inside and outside corner quadrants both show the same significant and insignificant correlations as the full transect means. Comparing the correlation coefficients between the two sides of the ridge axis shows that the across-axis differences in all but two of the coefficients are statistically insig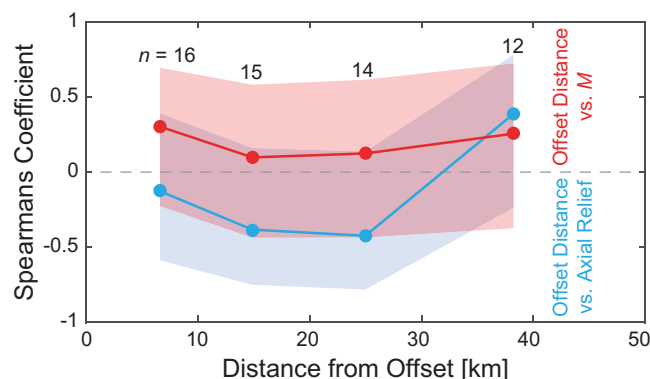nificant (Table 1a). Furthermore, the mean values of all the parameters do not differ significantly between the two sides of the axis (Table 1b). The two significant differences found are in the correlations of M and throw with distance to an offset: the correlation with M at inside corners is 1.6 times greater than that for the outside corners. Thus, mean M and fault throw do not differ significantly between the two sides of the ridge axis, but change more appreciably toward the inside corner than toward the outside corner.

Figure 10. Spearman's correlation coefficients and 95% confidence intervals for correlations between offset distance and M (red) and axial relief (blue). Correlations were calculated for transects in 10 km bins of along-axis distance from an offset; all distances ≥ 30 km were included in the same bin to maintain similar sample sizes. Data are plotted at the bin mean offset distance, and the plotted numbers show the sample size, n, contained in each bin. Confidence intervals for each bin cross zero, showing that within 95% confidence, there are no distinguishable relationships between offset distance and the estimated parameters at any point along the ridge segments.

4.6. Intersegment Variability and Sensitivity to Plate Boundary Geometry

To investigate differences between segments, we examine how measured variables change with offset distance and segment length. Comparing transect means of the northern and
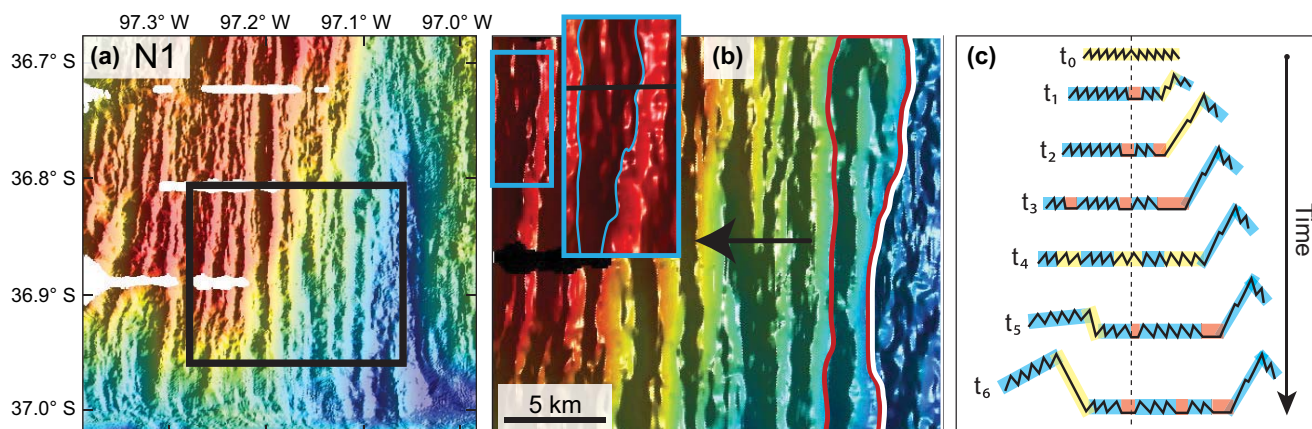
Figure 11. (a) Shaded relief map of segment N1 multibeam bathymetry. (b) Close-up of the black rectangle shown in Figure 11a. The black arrow shows the spreading direction. The white line in Figure 11b marks the western edge an area of diffuse deformation, where many small sinuous faults occur near the axis. As these small faults move away from the ridge axis, strain begins to concentrate on a few faults that link together along-axis and quickly grow into large abyssal-hill-scale faults (the youngest in this panel is outlined by red line). With continued seafloor spreading, the large fault stops slipping [*Behn and Ito*, 2008; *Buck et al.*, 2005] and diffuse extension on small faults accommodate the tectonic extension in the axial zone, beginning the process again. The small blue box shows the location of the subset enlarged footwall region of an older, now inactive abyssal hill-scale fault, which still preserves the small-scale axial fault fabric highlighted on the back of the fault. (c) Cartoon illustrating fault evolution with time. At time t_0, a ridge axis undergoes diffuse extension on short, small-throw, sinuous faults (fabric highlighted in yellow signifies active faults). At time t_1, small faults begin to link along the ridge axis, rapidly accumulating strain, and form an abyssal hill-scale fault by time t_3 that rafts abandoned axial fabric (fabric highlighted in blue signifies inactive faults) on the footwall. During this time, magmatic extension contributes to spreading (fabric highlighted in red). At time t_4, the abyssal hill-scale fault is inactive and the axis again undergoes diffuse extension, and the process repeats.

southern segment-halves (grouping 5) with the distance of the neighboring offset does not yield any significant correlations (Figure 7, row d). Further, means of transects grouped according to, d, the transect proximity to the segment end (groupings 1–4) do not show any significant correlations with offset distance (Figure 10). Correlations between ridge segment length and segment mean properties show that longer segments tend to exhibit less overall axial relief (Figure 7, row e), but are not significant for all the other properties. Together these results suggest that the impact of the plate boundary geometry on faulting, magmatism, and morphology is negligible at the Chile Ridge.

5. Discussion and Inferences

5.1. Geologic Mechanism of Fault Formation and Evolution

Close inspection of the seafloor fabric on and adjacent to the Chile Ridge provides insight into the evolution of faults and the origin of abyssal hills. Between the axially continuous, large abyssal hill fault scarp complexes, the seafloor is typically broken by numerous short strike, small faults (e.g., see Figures 11a and 11b). This pattern is ubiquitous, and can be explained by a new model of cyclic fault growth that is consistent with current concepts of fault initiation and interaction in three dimensions [e.g., *Carbotte and Macdonald*, 1994; *Cowie et al.*, 1993] and the mechanical limits on the width of the active fault zone near the ridge axis [*Behn and Ito*, 2008; *Buck et al.*, 2005; *Chen and Morgan*, 1990a].

At the onset of one of these faulting cycles, extension is accommodated within a few kilometers of the ridge axis through diffuse tectonic deformation on numerous small faults (Figures 11b and 11c, time t_0). With continued extension, some of these faults link, accommodating a disproportionate amount of the tectonic strain, and eventually grow into tall and long abyssal-hill-scale fault complexes (Figures 11b and 11c, times t_1-t_3). The large faults then raft the abandoned small faults away from the ridge axis on the back of the footwall. This inferred evolution is consistent with observations and numerical models of normal faults [e.g., *Cowie and Roberts*, 2001; *Dawers and Anders*, 1995; *Manighetti et al.*, 2015], in which continued slip and fault propagation cause many small faults to link along strike and form much longer and taller faults.

Eventually, the large fault moves far enough off axis and has accumulated enough slip that a greater force is required to keep it slipping than to initiate a new fault closer to the ridge axis [*Behn and Ito*, 2008; *Buck et al.*, 2005]. When this occurs, diffuse tectonic extension on small faults occurs near the ridge axis as before (Figure 11c, time t_4). The cycle repeats, with the next large fault typically forming on the opposite side of the ridge axis (Figure 11c, t_5-t_6). The result is periodically spaced, axis-parallel fault complexes superimposed

on the longer wavelength topography associated with the axial valley (e.g., Figure 3c). It is unclear whether this cycle occurs in discrete stages, as described, or whether multiple stages can be contemporary. We estimate that a new abyssal hill fault-complex generally forms at the Chile Ridge once every 220–340 kyr based on the spreading rate and mean spacing of the large-scale abyssal hill structures.

5.2. Changes in Magmatic Extension With Uniform Fault Spacing

The finding that fault spacing does not change systematically with any variables along the Chile Ridge indicates that the observed changes in M are accommodated by changes in mean fault throw, and not changes in fault frequency (i.e., spacing). A small seamount chain at N9N illustrates this behavior (Figures 1c and 6d—second transect from the top). Here throw decreases along individual faults as they approach the seamounts where M is anticipated to be locally very high. The decrease in fault throw is seen as a deepening of the tops of the faults toward the seamounts, indicating a reduction in total fault slip. This depression of fault scarp tops is not likely due to flexure of the lithosphere, given the small wavelength of the volcanoes relative to the elastic plate thickness [e.g., *Olive et al.*, 2015]. This observation is distinguishable from the alternative situation where magma infills the fault basins, whereby the fault bottoms would shoal and fault tops would remain at constant depth, and the topographic expression of throw would be reduced, but the true throw would not decrease.

We interpret these observations to indicate that the formation of the seamounts occurred near the axial zone of diffuse tectonic deformation and led to a locally high proportion of magmatic extension. In fact, M may have been close to 1 where the largest seamounts formed, as evident by the complete termination of the faults on either side of the seamounts (Figure 1c). Near the lower topographic bulge just east of the shorter seamount, the fault top deepens, but the fault continues through the bulge, suggesting M is locally high, but <1. This is an example of where a local high in magma flux correlates with a reduction in the amount of slip on the adjacent faults without a clear change in fault spacing.

To explain the lack of a change in fault spacing with proximity to segment offsets and M, we refer back to predictions of mechanical models of *Behn and Ito* [2008]. First, they show that the sensitivity of fault spacing on M rapidly decreases for high values of M. Given the relatively small magnitude of along-axis variations in M, it is possible that a dependency of fault spacing on M is present, albeit masked by natural variations in the fault population. Additional support for this possibility is that while M and fault spacing are not correlated at the 5% confidence level, they are correlated at the 10% confidence level.

Additionally, *Behn and Ito* [2008] showed that decreasing both M and the lithospheric thickness tends to increase fault spacing. We hypothesize that the observed decrease in M toward segment ends tends to increase fault spacing, while reduced magma delivery near segment ends results in cooler, thicker axial lithosphere and slower off-axis thickening rate, which tends to reduce fault spacing [*Behn and Ito*, 2008]. Thus, the relatively high and uniform values of M imply that only small variations in lithospheric thickness are required for the two counteracting effects to obscure any systematic variation in fault spacing. Finally, along-axis stress coupling, which was not addressed by *Behn and Ito* [2008], may be important, as the axis-parallel abyssal hill-scale faults can extend over a large fraction (25–60%) of the total segment length. The tendency of faults to preserve their along-axis integrity would tend to minimize changes in the spacing between faults with the relatively subtle changes in M along the segment.

Another finding for the Chile Ridge is that mean values of M and fault spacing do not differ significantly between inside corners and outside corners; it is only the change in M from segment centers toward inside corner offsets that appears to be greater than the change in M toward outside corner offsets. No such difference is apparent with fault spacing. These results contrast with those of *Escartín et al.* [1999], who showed little or no change in M along axis, but a significant increase in mean fault spacing and fault throw with proximity to the inside corner of a nontransform offset at Mid-Atlantic Ridge. This contrast indicates a difference in the mechanics of inside corners at that particular offset than along the Chile Ridge, and that the variations we observe in relatively high values of M may be too small to have a measurable effect on the segment corners.

5.3. Evidence for Mantle Controls on Ridge Segmentation

At the Chile Ridge, we find that all measured parameters, including M and segment morphology, vary independently of segment offset distance, and that only axial relief depends significantly on segment length. In addition, variations in axial valley relief, M, F, and the overall ridge structure indicate magmatic segmentation at a preferred length scale of 50 ± 20 km that can occur in the absence of tectonic segmentation. These

findings are two separate lines of evidence against plate boundary geometry, characterized by segment length and offset distances, exerting a primary control on along-axis variations in magmatism, faulting, and morphology at the Chile Ridge.

In one end-member case for mantle flow beneath a spreading axis, mantle upwelling is driven entirely as a passive response to the divergence of the overlying plates [e.g., *Parmentier and Phipps Morgan*, 1990]. In this "top-down" scenario, along-axis variations in mantle flow and magma flux are most tightly linked to the geometry of the plate boundary. For example, sections of ridge near the long transforms would have lower magma flux and lower M than those near short transforms, and magma flux and M would always be high in segment centers and increase with segment length. The predictions of this end-member form of mantle flow and melting are not consistent with our findings of the Chile Ridge.

Another end-member case for mantle flow involves active mantle upwelling driven by buoyancy contrasts resulting from perturbations in mantle melting or temperature, thus causing surface variations from the "bottom-up" [e.g., *Jha et al.*, 1994; *Lin and Phipps Morgan*, 1992; *Parmentier and Phipps Morgan*, 1990; *Sparks et al.*, 1993]. Our findings of a 50 ± 20 km segmentation in M, axial relief and F, and no correlation between the first two parameters with offset distance are better explained by the presence of active upwelling cells beneath the Chile Ridge. We propose that rapid upwelling in the centers of these cells tend to occur beneath segment centers, and the more slowly upwelling cell edges tend to coincide with segment ends. However, when spreading segments are much longer than the preferred wavelengths (50 ± 20 km) of the cells, the surface is imprinted with periodic along-axis variations, such as the stacked hourglass morphology of segment N9N. These variations in magmatism, faulting, and morphology, and the location of upwelling cells may even promote the later formation of segment offsets. For example, segment N9S, a third hourglass along segment N9, is offset from N9N where M is locally minimal, away from the proposed upwelling cell center. Thus, we argue for the bottom-up process whereby variations in magma supply from these upwelling cells control second-order segmentation [*Schouten et al.*, 1985] as opposed to the top-down process whereby segmentation imposes controls on magma supply [*Lonsdale*, 1989; *VanderBeek et al.*, 2014].

Evidence for a bottom-up control along the southern Chile Ridge and along the Southwest Indian Ridge comes from observations of intersegment distinctions in lava isotope compositions, which suggest that tectonic segments are segregated by differing mantle source compositions [*Meyzen et al.*, 2005; *Sturm et al.*, 1999]. Additionally, *Wilson et al.* [2013] propose that reduced melt production due to depleted mantle melting at slow spreading ridges can cause a transition from magmatic to amagmatic spreading at oceanic core complexes. These relationships between variations in melt supply, magmatic accretion, and ridge morphology hint at an underlying geochemical control on faulting, morphology, and ridge geometry that ultimately originates from within the mantle.

6. Conclusions

In this study, we characterized relationships between magmatic accretion inferred from tectonic strain (M), fault characteristics, ridge geometry, and axial morphology at the intermediate spreading Chile Ridge. At the intrasegment scale, we find that fault throw generally decreases toward the segment center, but that fault spacing does not change systematically along axis. Thus, an observed increase in M from segment ends to segment centers results in shorter throw, similarly spaced faults. This finding contrasts with the Mid-Atlantic Ridge, where fault spacing tends to be widest near segment ends and decreases toward segment centers. Additionally, while the along-axis increase in M toward segment centers may be slightly more pronounced at the inside corners of offsets, we find no significant across-axis variation in mean M or fault spacing between inside and outside corners.

Correlated along-axis variations in M, axial valley relief, and petrologic indicators of the fraction of partial melting of the mantle indicate a length scale of magmatic segmentation of $\sim 50 \pm 20$ km that persists independently of tectonic segmentation along the longest ridge segments. Further, we observe no systematic correlations between M and axial relief with adjacent transform and nontransform offset distances, and find that segment length correlates only with axial relief. Thus, rather than responding passively to plate separation, the mantle beneath the Chile Ridge likely exhibits magmatic segmentation due to deep-sourced variations in melt supply that result from segmented active mantle upwelling that is partly decoupled from the geometry of the plates.

We propose that abyssal hills near the Chile Ridge are created by an initial stage of diffuse tectonic extension near the ridge axis, followed by the linking of small faults to form large fault complexes that form the bounding structures of abyssal hills. These abyssal-hill-scale fault complexes raft packets of small, failed axial faults on their footwall, and are superimposed on the long-wavelength topography associated with the axial valley.

The systematic along-axis variations in M and axial morphology without corresponding changes in fault spacing demonstrate the inherently 3-D nature of mid-ocean ridge processes. These findings illuminate the need for detailed studies of bathymetry and ridge structure across all spreading rates, as well as 3-D numerical models of magmatic accretion and faulting, to advance our understanding of the relative importance of along-axis variations in M, stress coupling, and crustal temperatures on the structure of the seafloor created at mid-ocean ridges.

References

Behn, M. D., and G. Ito (2008), Magmatic and tectonic extension at mid-ocean ridges: 1. Controls on fault characteristics, *Geochem. Geophys. Geosyst.*, 9, Q08O10, doi:10.1029/2008GC001965.

Bohnsenstiehl, D. R., and S. M. Carbotte (2001), Faulting patterns near 19°30′S on the East Pacific Rise: Faults formation and growth at a superfast spreading center, *Geochem. Geophys. Geosyst.*, 2(9), 1056, doi:10.1029/2001GC000156.

Bohnenstiehl, D. R., and M. C. Kleinrock (1999), Faulting and fault scaling on the median valley floor of the trans-Atlantic geotraverse (TAG) segment, ~26°N on the Mid-Atlantic Ridge, *J. Geophys. Res.*, 104, 29,351–29,364.

Buck, W. R., L. L. Lavier, and A. N. B. Poliakov (2005), Modes of faulting at mid-ocean ridges, *Nature*, 434, 719–723.

Carbotte, S. M., and K. C. Macdonald (1994), Comparison of seafloor tectonic fabric at intermediate, fast, and super fast spreading ridges: Influence of spreading rate, plate motions, and ridge segmentation on fault patterns, *J. Geophys. Res.*, 99, 609–613.

Carbotte, S. M., D. Smith, M. Cannat, and E. Klein (2015), Tectonic and magmatic segmentation of the Global Ocean Ridge System: A synthesis of observations, *Geol. Soc. Spec. Publ.*, 420, doi:10.1144/SP420.5.

Chen, Y. J., and W. J. Morgan (1990a), Rift valley/no rift valley transition at mid-ocean ridges, *J. Geophys. Res.*, 95, 17,571–17,581.

Chen, Y. J., and W. J. Morgan (1990b), A nonlinear rheology model for mid-ocean ridge axis topography, *J. Geophys. Res.*, 95, 17,583–17,604.

Cowie, P. A., and G. P. Roberts (2001), Constraining slip rates and spacings for active normal faults, *J. Struct. Geol.*, 23, 1901–1915.

Cowie, P. A., C. H. Scholz, M. Edwards, and A. Malinverno (1993), Fault strain and seismic coupling on mid-ocean ridges, *J. Geophys. Res.*, 98, 911–917.

Dawers, N. H., and M. H. Anders (1995), Displacement-length scaling and fault linkage, *J. Struct. Geol.*, 17(5), 607–614.

Dunn, R. A., V. Lekic, R. S. Detrick, and D. R. Toomey (2005), Three-dimensional seismic structure of the Mid-Atlantic Ridge (35°N): Evidence for focused melt supply and lower crustal dike injection, *J. Geophys. Res*, 110, B09101, doi:10.1029/2004JB003473.

Escartín, J., P. A. Cowie, R. C. Searle, S. Allerton, N. C. Mitchell, C. J. MacLeod, and A. P. Slootweg (1999), Quantifying tectonic strain and magmatic accretion at a slow spreading ridge segment, Mid-Atlantic Ridge, 29°N, *J. Geophys. Res.*, 104, 10,421–10,437.

Forsyth, D. W. (1992), Finite extension and low-angle normal faulting, *Geology*, 20, 27–30.

Goff, J. A., Y. Ma, A. Shah, J. R. Cochran, and J.-C. Sempéré (1997), Stochastic analysis of seafloor morphology on the flank of the Southeast Indian Ridge: The influence of ridge morphology on the formation of abyssal hills, *J. Geophys. Res.*, 102, 15,521–15,534, doi:10.1029/1097JB00781.

Hooft, E. E. E., R. S. Detrick, D. R. Toomey, J. A. Collins, and J. Lin (2000), Crustal thickness and structure along three contrasting spreading segments of the Mid-Atlantic Ridge, 33.5°–35°N, *J. Geophys. Res.*, 105, 8205–8226.

Ito, G., and M. D. Behn (2008), Magmatic and tectonic extension at mid-ocean ridges: 2. Origin of axial morphology, *Geochem. Geophys. Geosyst.*, 9, Q09O12, doi:10.1029/2008GC001970.

Jha, K., E. M. Parmentier, and J. P. Morgan (1994), The role of mantle depletion and melt-retention buoyancy in spreading-center segmentation, *Earth Planet. Sci. Lett.*, 125, 221–234.

Karsten, J., et al. (1999), The northern Chile Ridge revealed: Preliminary cruise report of PANORAMA Expedition Leg 04, in *InterRidge News*, edited by C. Wilson, pp. 15–21, InterRidge Office, Paris, France.

Kuo, B.-Y., and D. W. Forsyth (1988), Gravity anomalies of the ridge-transform system in the South Atlantic between 31° and 34.5°S: Upwelling centers and variations in crustal thickness, *Mar. Geophys. Res.*, 10, 205–232.

Lin, J., and E. M. Parmentier (1989), Mechanisms of lithospheric extension at mid-ocean ridges, *Geophys. J.*, 96, 1–22.

Lin, J., and J. Phipps Morgan (1992), The spreading rate dependence of three-dimensional mid-ocean ridge gravity structure, *Geophys. Res. Lett.*, 19, 13–16.

Lin, J., G. M. Purdy, H. Schouten, J.-C. Sempéré, and C. Zervas (1990), Evidence from gravity data for focused magmatic accretion along the Mid-Atlantic Ridge, *Nature*, 344, 627–632.

Lonsdale, P. (1989), Segmentation of the Pacific-Nazca Spreading Center, 1°N-20°S, *J. Geophys. Res.*, 94, 12,197–12,225.

Macdonald, K. C. (1982), Mid-ocean ridges: Fine scale tectonic volcanic and hydrothermal processes within the plate boundary zone, *Annu. Rev. Earth Planet. Sci.*, 10, 155–190.

Macdonald, K. C. (1986), The crest of the Mid-Atlantic Ridge: Models for crustal generation processes and tectonics, in *The Geology of North America*, edited by P. R. Vogt and B. E. Tucholke, pp. 51–68, Geol. Soc. of Am., Boulder, Colo.

Macdonald, K. C., D. S. Scheirer, and S. M. Carbotte (1991a), Mid-Ocean ridges: Discontinuities, segments and giant cracks, *Science*, 253, 986–994.

Manighetti, I., C. Caulet, L. De Barros, C. Perrin, F. Cappa, and Y. Gaudemer (2015), Generic along-strike segmentation of Afar normal faults, East Africa: Implications on fault growth and stress heterogeneity on seismogenic fault planes, *Geochem. Geophys. Geosyst.*, 16, 443–467, doi:10.1002/2014GC005691.

Meyzen, C. M., J. N. Ludden, E. Humler, B. Luais, M. J. Toplis, C. Mével, and M. Storey (2005), New insights into the origin and distribution of the DUPAL isotope anomaly in the Indian Ocean mantle from MORB of the Southwest Indian Ridge, *Geochem. Geophys. Geosyst.*, 6, Q11K11, doi:10.1029/2005GC000979.

Milman, M. S. (2002), *Petrogenesis of Lavas From the Axis of the Northern Chile Ridge*, 143 pp., Univ. of Hawaii at Manoa, Honolulu.

Olive, J.-A., and M. D. Behn (2014), Rapid rotation of normal faults due to flexural stresses: An explanation for the global distribution of normal fault dips, *J. Geophys. Res. Solid Earth*, *119*, 3722–3739, doi:10.1002/2013JB010512.

Olive, J.-A., J. Escartín, M. Behn, W. R. Buck, G. Ito, and S. M. Howell (2015), Sensitivity of seafloor bathymetry to climate-driven fluctuations in mid-ocean ridge magma supply *Science*, *350*(6258), 310–313.

Parmentier, E. M., and J. Phipps Morgan (1990), Spreading rate dependence of three-dimensional structure in oceanic spreading centres, *Nature*, *348*, 325–328.

Paulatto, M., J. P. Canales, R. A. Dunn, and R. A. Sohn (2015), Heterogeneous and asymmetric crustal accretion: New constraints from multibeam bathymetry and potential field data from the Rainbow area of the Mid-Atlantic Ridge (36°15′N), *Geochem. Geophys. Geosyst.*, *16*, 2994–3014, doi:10.1002/2015GC005743.

Phipps Morgan, J., and Y. J. Chen (1993a), The genesis of oceanic crust: Magma injection, hydrothermal circulation, and crustal flow, *J. Geophys. Res.*, *98*, 6283–6297.

Phipps Morgan, J., and Y. J. Chen (1993b), Dependence of ridge-axis morphology on magma supply and spreading rate, *Nature*, *364*, 706–708.

Schouten, H., K. D. Klitgord, and J. A. Whitehead (1985), Segmentation of mid-ocean ridges, *Nature*, *317*, 225–229.

Schouten, H., D. K. Smith, J. R. Cann, and J. Escartín (2010), Tectonic versus magmatic extension in the presence of core complexes at slow-spreading ridges from a visualization of faulted seafloor topography, *Geology*, *38*(7), 615–618.

Searle, R. C., and A. S. Laughton (1981), Fine-scale study of tectonics and volcanism on the Reykjanes Ridge, *Oceanol. Acta*, *4*, 5–18.

Shaw, P. R. (1992), Ridge segmentation, faulting and crustal thickness in the Atlantic Ocean, *Nature*, *358*, 491–493.

Shaw, P. R., and J. Lin (1993), Causes and consequences of variations in faulting style at the Mid-Atlantic Ridge, *J. Geophys. Res.*, *98*, 21,839–21,851.

Shaw, W. T., and J. Lin (1996), Models of oceanic ridge lithospheric deformation: Dependence on crustal thickness, spreading rate, and segmentation, *J. Geophys. Res.*, *101*, 17,977–17,993.

Small, C. (1998), Global systematics of mid-ocean ridge morphology, in *Faulting and Magmatism at Mid-Ocean Ridges*, edited by R. W. Buck et al., pp. 1–25, AGU, Washington, D. C.

Sparks, D. W., E. M. Parmentier, and J. P. Morgan (1993), Three-dimensional mantle convection beneath a segmented spreading center: Implications for along-axis variations in crustal thickness and gravity, *J. Geophys. Res.*, *98*, 21,977–21,995.

Sturm, M. E., E. M. Klein, D. W. Graham, and J. Karsten (1999), Age constraints on crustal recycling to the mantle beneath the southern Chile Ridge: He-Pb-Sr-Nd isotope systematics, *J. Geophys. Res.*, *104*, 5097–5114.

Tapponnier, P., and J. Francheteau (1978), Necking of the lithosphere and the mechanics of slowly accreting plate boundaries, *J. Geophys. Res.*, *83*, 3955–3970.

Tebbens, S. F., S. C. Cande, L. Kovaks, J. C. Parra, J. L. LaBrecque, and H. Vergara (1997), The Chile ridge: A tectonic framework, *J. Geophys. Res.*, *102*(B6), 12,035–12,059.

Tolstoy, M., A. J. Harding, and J. A. Orcutt (1993), Crustal thickness on the Mid-Atlantic ridge: Bull's eye gravity anomalies and focused accretion, *Science*, *262*, 726–729.

Tucholke, B. E., M. D. Behn, W. R. Buck, and J. Lin (2008), Role of melt supply in oceanic detachment faulting and formation of megamullions, *Geology*, *36*(6), 455–458.

VanderBeek, B., D. R. Toomey, E. E. E. Hooft, and W. S. D. Wilcock (2014), Segment-scale seismic structure of slow-, intermediate-, and fast-spreading mid-ocean ridges: Constraints on the origin of ridge segmentation and the geometry of shallow mantle flow, Abstract V23E-07 presented at the 2014 Fall Meeting, AGU, San Francisco, Calif., 15–19 Dec.

Webb, H. F., and T. H. Jordan (2001), Pelagic sedimentation on rough seafloor topography: 1. Forward Model, *J. Geophys. Res.*, *106*, 30,433–30,449.

Wilson, S. C., B. J. Murton, and R. N. Taylor (2013), Mantle composition controls the development of an Oceanic Core Complex, *Geochem. Geophys. Geosyst.*, *14*, 979–995, doi:10.1002/ggge.20046.